Tropopause laminar cirrus and its role in the lower stratosphere total water budget

Tao Wang[1,2], Dong L. Wu[2], Jie Gong[2,3], Victoria Tsai[4]

[1] Earth System Science Interdisciplinary Center, University of Maryland, College Park, Maryland

[2] Earth Sciences Division, NASA Goddard Space Flight Center, Greenbelt, Maryland

[3] Universities Space Research Association, Columbia, Maryland

[4] Stanford University, Stanford, California

Correspondence to: Tao Wang (Tao.Wang@nasa.gov)

Key Points

- Laminar cirrus accounts for 30-40% of the total cirrus at the tropopause
- Laminar cirrus frequency and associated ice are anti-correlated with temperature and water vapor (H_2O) seasonally and interannually
- Laminar cirrus is a direct response to the tropopause temperature via nucleation of available H_2O sourced from ambient air

Abstract

Laminar cirrus are thin, extensive, isolated layers of ice clouds frequently observed in the tropical tropopause layer (TTL). Widespread laminar cirrus significantly affects TTL total water and thermal budget. In this study, we extract laminar cirrus from the CALIOP L1 attenuated total backscatter images for January 2009, in order to characterize statistical properties of laminar cirrus cloud length, base, thickness, optical depth, and layer partial ice water path. These characteristics are used to develop an algorithm identifying laminar cirrus automatically from the CALIOP L2 layer product for 2008-2017. The nearly ten-year records reveal that tropopause laminar cirrus occurrence (30-40% of total cirrus) is strongly anticorrelated with the tropopause temperatures in that colder tropopause in

frequent (super)saturation during boreal winter favors *in situ* formation of clouds. Interannually, anomalously warmer troposphere temperature (ΔT), easterly shear of the quasi-biennial oscillation (QBO), and stronger upwelling branch of the Brewer-Dobson circulation (BDC) enhance laminar cirrus formation via cooling of the tropopause. The tropopause laminar cirrus carries ~0.05 mg/m^3 (~0.5 ppmv) of ice water content (IWC) during boreal winter and <0.01 mg/m^3 during summer, which is anticorrelated with the seasonal variations of water vapor (H_2O) observed by the MLS, indicating a temperature-regulated partition between vapor and ice. Interannually, in cirrus-rich region 1 ppmv decrease in H_2O corresponds to 0.2-0.3 ppmv increase in IWC. Frequently situated in (super)saturated air, tropopause laminar cirrus are likely to survive multiple lifecycles of the sublimation-deposition processes, and may contribute up to 10% to the total water budget in the lower stratosphere.

Plain Language Summary

Satellites constantly observe thin, isolated, extensive layer of cirrus around the tropopause. The so-called “laminar” cirrus occurrence and their ice amount are strongly regulated by temperature, such that colder temperatures favor more frequent (super)saturation, which results in more frequent laminar cirrus with more ice amount, and therefore less water vapor. In this study we analyze laminar cirrus and water vapor from the CALIOP and MLS observations, and hypothesize that laminar cirrus could act as an important transient water storage and contribute to the total water budget in the lower stratosphere.

1. Introduction

Cirrus are thin, ice clouds frequently observed in the tropical tropopause layer (TTL, ~14-19 km) – a transition layer between the convectively driven troposphere and the radiatively driven stratosphere. The TTL is characterized by large-scale slow ascent of air, where the dehydrated air favors *in situ* formation of cirrus [*Fueglistaler et al.*, 2009 and references therein], and the dehydration process regulates the amount of water vapor (H_2O) entering the stratosphere [*Danielsen*, 1993; *Jensen et al.*, 1998; *Jensen and Pfister*, 2004]. The TTL cirrus therefore affects the total water vapor budget by storing a considerable amount of water in the condensed phase and transporting, scavenging, and sublimating ice particles on a global scale [e.g., *McFarquhar et al.*, 2000; *Jensen et al*., 2013; *Schoeberl et al.*, 2014]. TTL cirrus also significantly affects the thermal and radiation budget of the atmosphere [e.g., *Zhou et al.*, 2014].

Laminar cirrus, a subset of TTL total cirrus, is thinner, more extensive, long-lived cirrus; often isolated from thick anvil cirrus that is of directly convective origin [*Wang and Dessler*, 2012]. Their long extension, sometimes over thousands of kilometers, make them readily distinguishable in the lidar measurements [*Winker and Trepte*, 1998]. Laminar cirrus prevails in the TTL especially near the tropopause [*Jensen et al.*, 1996; *Winker and Trepte*, 1998; *Pfister et al.*, 2001]. By definition, laminar cirrus remains difficult to observe globally with nadir-view passive sensors due to their subvisible, semi-transparent nature. Therefore, the extent to which laminar cirrus dehydrates the TTL and how much it contributes to the total TTL water budget has not been well quantified, and it remains an active research topic in understanding the TTL processes [e.g., *Immler et al.*, 2008; *Luo et al.*, 2003; *Martins et al.*, 2011; *Reverdy et al.*, 2012].

78 The Cloud-Aerosol Lidar with Orthogonal Polarization (CALIOP) onboard the
79 CALIPSO satellite provides an unprecedented record of TTL cirrus since the launch in
80 April 2006 [*Winker et al.*, 2007]. The CALIOP near-nadir viewing two-wavelength
81 polarization lidar is able to detect thin cirrus layers with optical depth (τ) as low as 0.001
82 [*McGill et al.*, 2007]. In terms of optical depth, laminar cirrus is similar to the subvisible
83 cirrus (common definition of optical depth < 0.03 [*Sassen et al.*, 1989]). In a large-scale
84 uplift saturated environment [*Corti et al.*, 2006], laminar cirrus forms as local temperature
85 is modulated by perturbations associated with gravity/Rossy/Kelvin wave activity [e.g.,
86 *Potter and Holton*, 1995; *Boehm and Verlinde*, 2000; *Pfister et al.*, 2001; *Garrett et al.*,
87 2004].

88 In this study we focus on the thin (~1 km), laminar cirrus layers that form in-situ in
89 the TTL and away from deep convection, with a horizontal span over a few hundred
90 kilometers. A great challenge with cloud detection algorithms is to accurately record the
91 aspect ratio of laminar cirrus structures. While it might appear continuous to human eyes,
92 laminar cirrus sometimes is reported by cloud detection algorithms as broken clouds, which
93 make it confused as short-scale anvil. As shown in **Fig. 1,** it is not reliable to discriminate
94 laminar cirrus solely based on horizontal lengths since the broken, upper-level cirrus could
95 yield several sections of clouds (marked as A) that have a similar length as the anvil outflow
96 (marked as B) near the deep convection. **Fig.1** also reveals a two-layer cirrus structure at
97 the tropopause coldest temperatures of < -80^{o}C, as indicated by the MERRA2 (Modern-
98 Era Retrospective analysis for Research and Applications, Version 2, *Gelaro et al.*, 2017].
99 The two layers of clouds have geometric thickness between 0.4-1.8 km, and of different
100 backscatter intensities that indicative of different densities of ice particles. While the lower-
101 level high-density layer (marked as C) is subject to loss of ice particles through

sedimentation, the upper-level low-density layer of cirrus (A) is expected to have a longer lifetime [*Jensen et al.*, 1996; *Garrett et al.*, 2004; *Dinh et al.*, 2010; *Taylor et al.*, 2011]. The cirrus-induced radiative heating is able to further self-maintain the cloud while going through multiple sublimation-deposition lifecycles in the TTL [*Gage et al.*, 1987; *Lilly*, 1998; *Dinh* et al., 2010]. It remains unclear to what extent that laminar cirrus could effectively interchange mass with water vapor (H_2O).

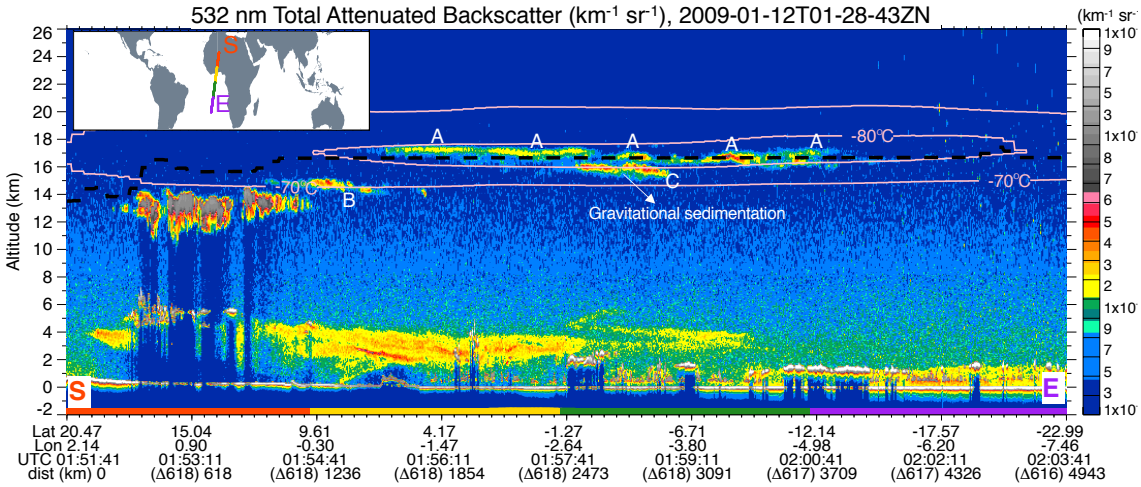

Figure 1. Laminar cirrus observed by CALIOP on Jan 12, 2009 in a ~15 min sector from 01:51'-02:03' UTC when crossing the South Atlantic Ocean region. The tropopause is marked in dashed black line and the temperatures at -70°C and -80°C are contoured in light red. This upper-level, low-density laminar cirrus (marked as A) has an overall horizontal extension of ~1260 km, but is shown broken into several sections of cloud of similar length as the anvil outflow (marked as B). The lower-level, high-density cloud (marked as C) is subject to loss of ice particles through sedimentation. Four horizontal bars in red, yellow, green, and violet marks the starting (S) and ending (E) time of the track separated equally into four segments of ~618 km each.

This paper provides an in-depth analysis of the 10-year laminar cirrus frequency and associated ice amount observed by the CALIOP. Combined with the MERRA-2 reanalysis and the MLS (Microwave Lime Sounder) observation of H_2O, we investigate the linkage between laminar cirrus ice and the total H_2O budget in the tropopause and the lower stratosphere. Different from previous studies that focused on the relationship to total cirrus [*Fu*, 2013; *Flury et al.*, 2012], we focus on the relations to thin, extensive, and isolated laminar cirrus layers. We develop two methods to identify laminar cirrus from the

CALIOP measurements: manual-selection and auto-selection. Described in section 2.1, the manual-selection method is human-aid cloud detection technique to digitize distinct layers of thin, extensive, and isolated laminar cirrus. It is applied only to one month (January 2009) of CALIOP level-1 (L1) attenuated total backscatter. Based on the one-month statistics of the physical properties of manually-selected laminar cirrus, an automatic algorithm is developed and applied to the CALIOP level-2 (L2) merged (cloud+aerosol) layer product for 2008–2017 (section 2.2). The morphology and connection between laminar cirrus frequency, laminar cirrus ice, and H_2O variability are investigated using the auto-selection of laminar cirrus (section 3), followed by discussions on the implication of the results in section 4, and a summary in section 5.

2. Data and Methods

CALIOP data in version 4 of both L1 (L1-Standard-V4-10, *Kar et al.*, [2018]) and L2 (05kmMLay-Standard-V4-20, *Liu et al.*, [2019]) are used for the TTL laminar cirrus study. Unlike microwave (CloudSat 94 GHz profiling radar and passive MLS limb sounding) techniques [*e.g., Stephens et al.*, 2002; *Wu et al.*, 2005], CALIOP is much more sensitive to thin cirrus layers in the TTL [e.g., *Riihimaki and McFarlane*, 2010; *Martin et al.,* 2011; *Wang et al.*, 2012].

2.1 Manual-selection method

The manual-selection method digitizes isolated, extensive, thin layers of cirrus directly distinguishable from the CALIOP L1 532-nm attenuated total backscatter (β'_{532}) image. This method is applied to January 2009 to obtain a month's laminar cirrus that are distinct from the background atmosphere and the ambient thick clouds. For each selected

layer of laminar cirrus, we record the starting/ending time counted to seconds and the associated cloud base and top at the middle point. The rationale for such approach is that human-eyes are still by far the most "intelligent" tool to identify the weakest signal and smart enough to connect disconnected profiles into one cloud so the morphology can be studied further.

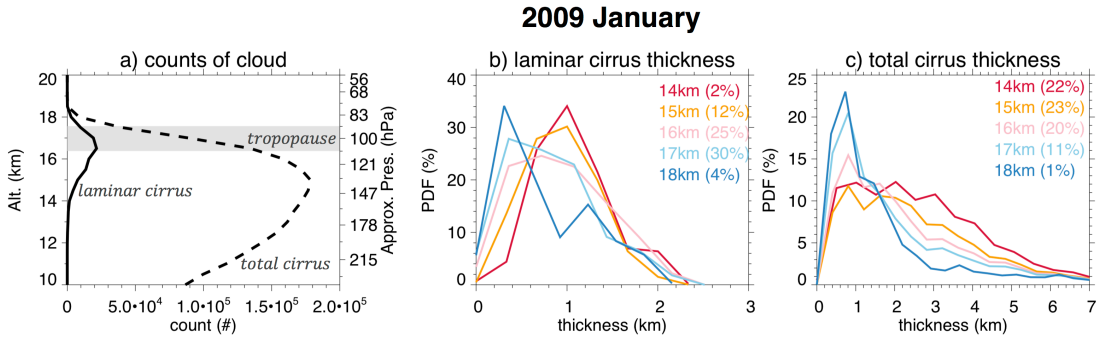

Figure 2. (a) Comparison of laminar cirrus (solid) and total cirrus (dashed) profiles; the probability density function (PDF) of (b) laminar cirrus thickness and (c) total cirrus thickness in function of height.

To better distinguish laminar cirrus from the total cirrus, we plot in **Fig. 2a** the occurrence profile of the laminar cirrus (solid) comparing to the total cirrus (dashed) averaged over the tropics (30° N–S). Here, total cirrus refers to all cloudy scenes being categorized as "cirrus" by the CALIOP scene classification algorithm, so that the occurrence of total cirrus > laminar cirrus. It is obvious that laminar cirrus mostly occurs at the tropopause level (~17 km or ~100 hPa) where air is the coldest, whereas total cirrus – including those thick anvil ones, peak at the bottom of TTL (~15 km or ~140 hPa) due to more influence from convections. This verifies that laminar cirrus *mostly* forms in situ in colder temperatures. Therefore, laminar cirrus are generally very thin (thickness between 0.3-1 km, **Fig. 2b**), whereas the thickness spectrum for total cirrus is much broader, with more thicker layers more frequently exist in lower altitudes (**Fig. 2c**) where ice crystals grow larger and fall faster, deepening the cloud layers.

158 For the manual selection of laminar cirrus, post processing is conducted to derive
159 their layer optical depth (τ) and layer partial ice water path (pIWP). First, we calculate
160 backscattering due to cloud particles (β'_{532p}) by removing attenuations by molecules and
161 ozone from β'_{532} [*Vaughn, et al.*, 2009]. Then, we calculate τ as function of layer integrated
162 backscatter coefficient γ_{Ci}' in sr^{-1} (*Eqn.* 3.14 in *Vaughn, et al.*, [2005]) following *Platt*
163 [1973]

164 $$\tau = -\frac{1}{2\eta}\ln(1 - 2\eta S\gamma'_{Ci}). \quad (1)$$

165 where η is the multiple scattering coefficient, defined as the ratio of the apparent
166 experimental visible extinction coefficient to the true visible extinction coefficient, and S
167 is the lidar ratio. As in *Martins et al.* [2011], we use $S = 25sr$ and $\eta = 0.7$ for thin cirrus
168 clouds. Last, we calculate pIWP based on empirical linear relation between cloud ice water
169 content (IWC) and lidar backscatter (IWC ≈ 0.61 x β'_{532p}, *Wu et al.*, [2014]). This relation
170 holds when cirrus IWC < 10 mg/m^3.

171 The manual-selection provides reliable characterization of the structural properties
172 of laminar cirrus. Statistical results show that the laminar cirrus has an average horizontal
173 extent of ~560 km, ranging from the least extensive case of 60 km to the most extensive
174 one stretching ~3000 km. On a profile-by-profile basis, the laminar cirrus layers have base
175 between 12-18 km (**Fig. 3a**), geometric thickness between 0.2-2.5 km (**Fig. 3b**), τ < 0.3
176 (the threshold for thin cirrus, **Fig. 3c**), and pIWP of 0.001-1 g/m^2 (**Fig. 3d**). More frequently,
177 the base of laminar cirrus is between 15-17 km (below the tropopause height of ~17±0.6
178 km, grey shading in **Fig. 3a**) and the geometric thickness is between 0.5-1 km – consistent
179 with the pioneer study from the Lidar In-space Technology Experiment (LITE, *Winker and*
180 *Trepte*, [1998]). About 80% of laminar cirrus has cloud top below the tropopause and cloud
181 τ < 0.03 (subvisible, [*Sassen et al.*, 1989]). According to the IWP and τ relations for particle

size in homogeneous formation (e.g., *Wang et al.* [2011]), the effective radius of these layered cirrus is less than 6 μm, which favors self-maintenance of hours to days [e.g., *Dinh et al.*, 2010]. The cumulative distribution function (CDF, right y axis) shows that almost all laminar cirrus clouds have 1) base ≥ 14 km, 2) thickness ≤ 2 km, 3) $\tau \leq 0.3$ (threshold for thin cirrus), and 4) layer pIWP ≤ 1 g/m^2. Those criteria will be used in our auto-selection of laminar cirrus described in the next section.

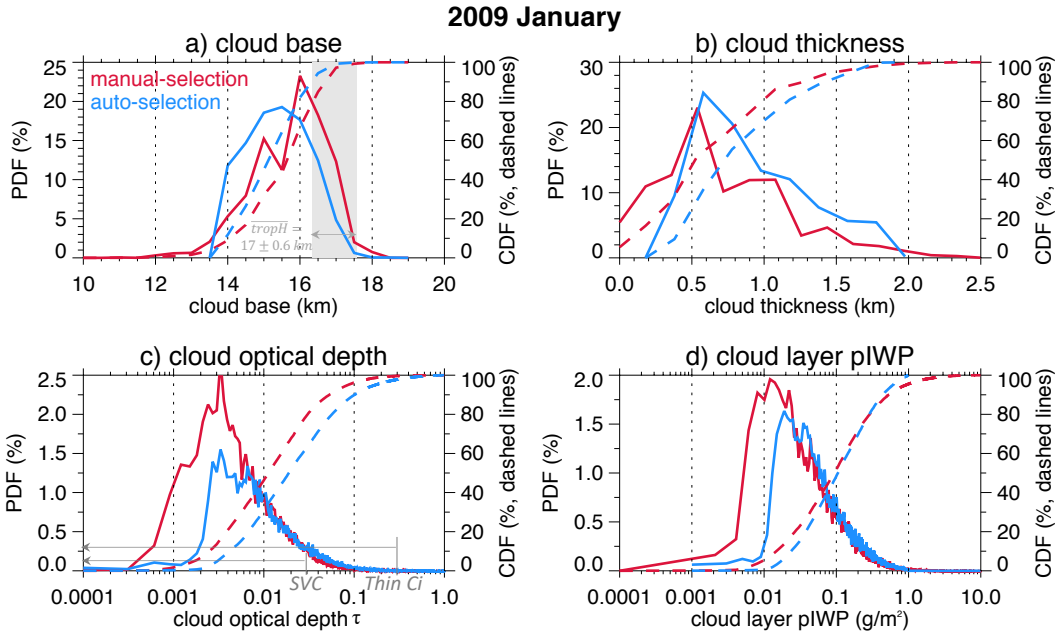

Figure 3. On profile basis, comparison of the PDF (probability density function, solid lines) and CDF (cumulative distribution function, dashed lines) of laminar cirrus a) base, b) geometric thickness, c) optical depth, and d) layer pIWP from both manual-selection (red) and auto-selection (blue) for January 2009. In panel a) the grey shading marks the tropopause height ± 1σ, and in panel c) the subvisible Ci (SVC, $\tau \leq 0.03$) and thin Ci ($\tau \leq 0.3$) are marked for reference.

2.2 Auto-selection method

Because the manual-selection is too labor-consuming to be applied for the entire CALIOP records, it is imperative to develop a fast, algorithm-based method that can be used on the CALIPSO L2 merged (cloud+aerosol) layer product (MLay), which separates the TTL clouds from aerosol layers ideally [*Vaughan et al.*, 2009; *Liu et al.*, 2019]. In this method we target those cirrus layers reported by the bit-based vertical feature mask (VFM)

195 [*Vaughan et al.*, 2005]. The 5-km product is preferred for cirrus research because of its
196 higher signal-to-noise ratio in detecting thin ice clouds [*Marchant et al.*, 2016].

197 The laminar properties from manual-selection provide key guidance for the
198 algorithm-based auto-selection of laminar cirrus. Besides the four criteria (i.e., base ≥ 14
199 km, thickness ≤ 2 km, $\tau \leq 0.3$, layer pIWP ≤ 1 g/m^2) mentioned in section 2.1, the auto-
200 selection algorithm requires thin cirrus layers to be at least 500 km away from any deep
201 convective (opaque) layers – if there is any, at the same altitude level, so as to exclude
202 cirrus formed directly from convective outflow. This requirement eliminates about 35% of
203 total thin cirrus in the L2 MLay data. In other words, approximately one third of thin cirrus
204 are probably associated with anvil outflows from deep convective systems. However, note
205 that the CALIOP meridional curtain cannot eliminate the cases where deep convective
206 towers are nearby but outside the satellite track. Another requirement is that the 5-km
207 profiles indicating existence of laminar cirrus to be continued for at least 60 km along track
208 (the lower threshold from L1 statistics), in an aim for picking relatively long, extensive
209 layer of cirrus.

210 For each auto-selected laminar cirrus, we record the same properties including layer
211 base and top, layer τ, and pIWP on profile-by-profile basis directly provided by the L2
212 MLay product. **Fig. 3** shows that statistics from the auto-selection (blue) method agrees
213 reasonably well with that from the manual-selection (red) method, with spectra showing
214 peak frequency in consistent range. However, we noticed subtle differences in τ and pIWP
215 at the lower end, which should be attributable to the different retrievals used for L1 and L2
216 data. For example, the pIWP calculated from L1 data is based on empirical relation of IWC
217 and β'_{532p} [*Wu et al.*, 2014], while the pIWP calculated from L2 data is based on
218 temperature-dependent relation between IWC and extinction coefficient (*Heymsfield et al.*,

219 [2014]). Other than this, the consistent PDFs of key physical properties from auto-selection
220 provides us confidence for a fast processing of longer laminar cirrus records.

221 Note that although laminar cirrus appears often obvious in the CALIOP backscatter
222 images, it is still challenging for the auto-selection method to detect and retain full layer
223 properties such as length accurately. The difficulties arise in cases where clouds are broken
224 due to density fluctuations, a layer is marginally separated from another below/above, or
225 clouds are horizontally too short to be considered as a layer. While the algorithms
226 developed in this study will not meet all requirements for characterizing laminar cirrus,
227 they should detect the majority of laminar cirrus and distinguish them from thick anvil
228 cirrus.

229

230 **2.3 MLS H_2O data**

231 To investigate the TTL H_2O-ice relation to the total water budget, we collocate
232 CALIOP laminar cirrus to the simultaneous MLS H_2O measurements from the A-Train
233 constellation. The latest version (v4.2) of MLS Level-2 data are used, including H_2O [*Read*
234 *et al.*, 2007; *Lambert et al.*, 2007], temperature [*Schwartz et al.*, 2008], geopotential height
235 [*Schwartz et al.*, 2008], and relative humidity with respect to ice (RHi) [*Read et al.*, 2007].
236 The reporting grid of MLS retrievals is ~168 km along track, resulting as many as 33
237 consecutive CALIPSO 5-km profiles within a single MLS profile for the same volume of
238 atmosphere. Vertically, we use the least square linear fit to interpolate MLS data from 12
239 to 36 levels per decade change in pressure (see MLS v4.2 quality document at
240 https://mls.jpl.nasa.gov/data/v4-2_data_quality_document.pdf) to better collocate MLS to
241 CALIOP observations. Around the tropopause between 121 and 68 hPa, this interpolation
242 yields MLS data at ~1 km interval vertically. Within this vertical range, MLS H_2O has a

243 precision of 5-20% and an accuracy of 8-12% from systematic errors. All data are screened
244 strictly following the recommendations of v4.2 quality document.

245 The formation of laminar cirrus layers is complex in general. To give an example,
246 **Fig. 4** shows a laminar cirrus from manual-selection enclosed in black boxes in **Fig.4a** and
247 from auto-selection shaded in blue in **Fig.4b**, comparing to the collocated MLS H_2O
248 marked in red dots in **Fig. 4c**. The two layers of laminar cirrus extend horizontally for
249 ~1400 km each. Fig. 4a shows that the enhancement of backscatter signals above the
250 molecular background is small for both layer of cirrus, due to small particles as well as
251 small number concentrations. Measurement above the tropopause (3^o N–S) indicates that
252 dehydration rapidly depletes H_2O to less than 2-3 ppmv (cyan and light blue in **Fig. 4c**),
253 relaxing ice saturation to ~100%. There is broad consistency between the laminar cirrus
254 identified by the two methods, but the manual-selection cannot outline the detailed cirrus
255 structures in small scales, whereas the auto-selection may likely miss tenuous layers by
256 relying on the cloud boundaries in layer product.

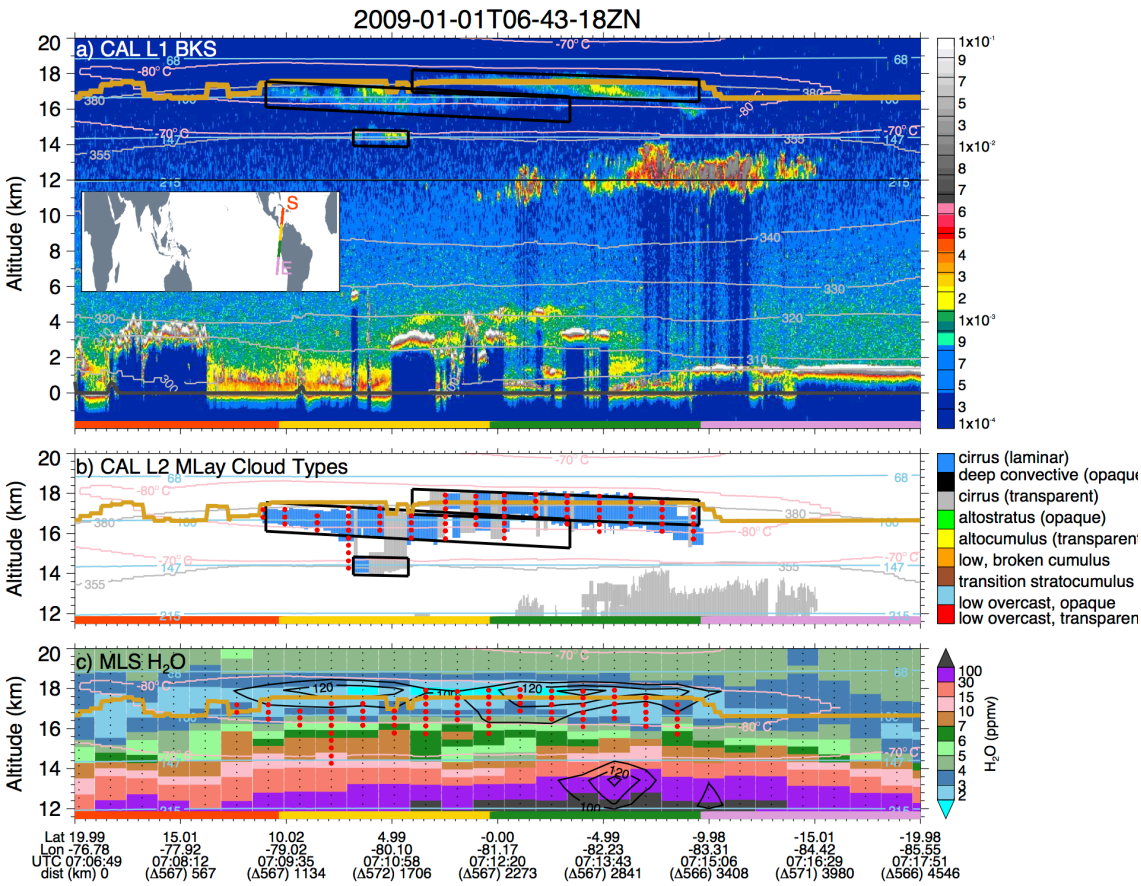

Figure 4. An illustration on January 1, 2009. a) CALIPSO L1 attenuated total backscatter (β'_{532}), with manual-selection of laminar cirrus encircled by black rectangles; b) CALIPSO L2 merged layer product indicating presence of cirrus layer (grey), with auto-selection of laminar cirrus highlighted in blue shading; c) MLS H_2O with center of grids marked in small black dots and collocated observations highlighted by red dots. The black boxes in panel a) and red dots in panel c) are repeated at panel b) for convenient comparison. The thick dark yellow line marks the tropopause. The black contours in panel c) are the relative humidity with respect to ice (RHi) in 100%, 120%, and 140%. For easy visualization, in each panel we use different colors to draw the isobars (215, 147, 100, 68 hPa), isotherms (-70 and -80 °C), and isentropes (355, 380, 425 K). The four horizontal bars in red, yellow, green, and violet at bottom of each panel marks the satellite track separated into four equal segments of ~1150 km each. The two laminar cirrus layers have horizontal lengths of ~1400 km.

The auto-selection method has advantage for computational efficiency, with which we are able to produce a nearly 10-year record of laminar cirrus in 2008-2017 in just a few days. We chose to start from May 2008 because 1) CALIPSO began to collocate its sampling with Aura MLS within 1 minute along the A-Train since then [*Wu et al.*, 2009]; and 2) CALIOP lidar has been operated consistently at 3° off-nadir angle in order to avoid

excessive amount of large backscattering due to horizontally oriented ice crystals [e.g., *Zhou et al.*, 2012].

3. Results

3.1. Laminar cirrus frequency

In this section we examine the frequencies of total cloudy, total cirrus, and laminar cirrus observed by the CALIOP. Total cloudy refers to all scenes identified by the CALIOP VFM as "cloud"; total cirrus refers to all cloudy scenes further categorized as "cirrus"; laminar cirrus refers to those cirrus layers that meets our criteria mentioned in section 2.1. Here, all frequencies are determined by the fraction of time that a scene is present along the CALIPSO overpass, so the frequencies of total cloudy > total cirrus > laminar cirrus.

There is overall consistent spatial pattern of the tropopause-level (100 hPa) laminar cirrus identified by two methods for January 2009 (**Fig. 5a-b)**. Both total cirrus (**Fig. 5c**) and laminar cirrus are confined within the tropics of 20^{o} N–S. Regionally, total cirrus occurs as frequently as > 60% over the Tropical Pacific, whereas laminar cirrus, as a subset of total cirrus, occur as frequently as >25% in the west/central of Pacific, equatorial western Africa, and northern South America.

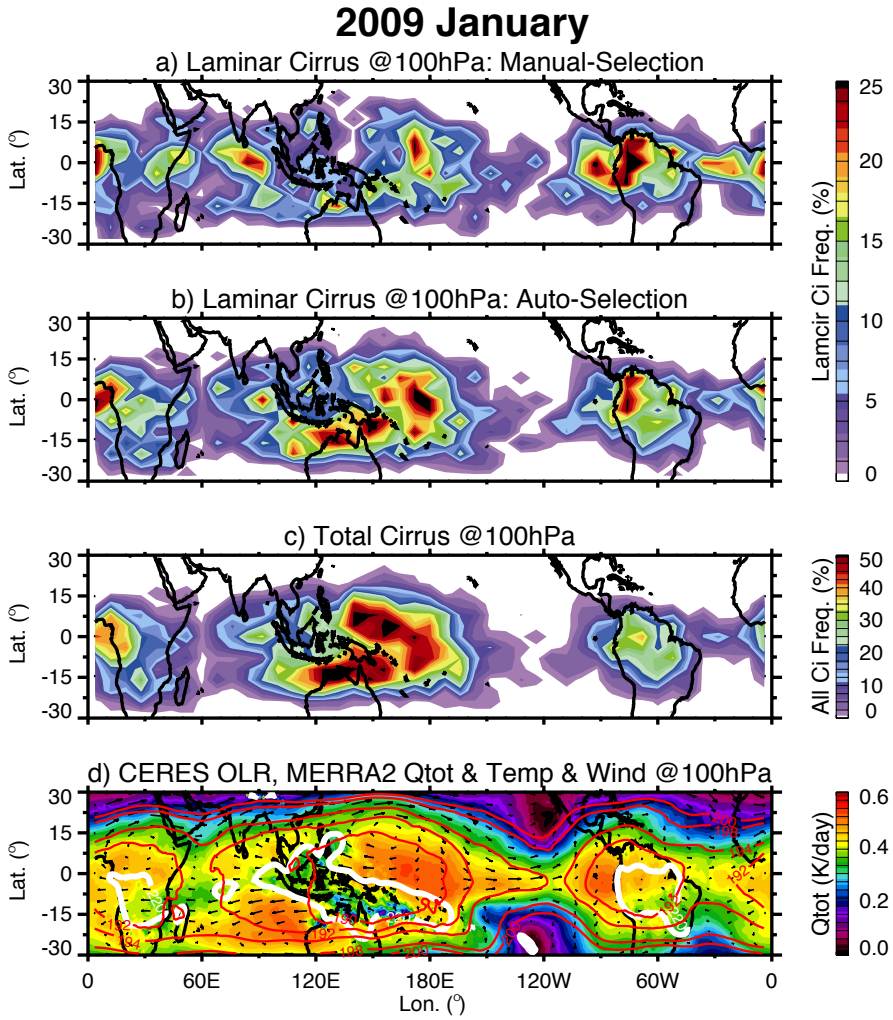

Figure 5. Laminar cirrus frequency at 100-hPa based on a) manual-selection and b) auto-selection; c) total cirrus frequency at 100-hPa; d) MERRA-2 total diabatic heating rates (color shading), temperatures (red contours), and wind at 100-hPa comparing to CERES OLR<220 W/m^2 (white contours). All data are from January 2009, with local frequency with respect to total observations within each grid for this month.

Laminar cirrus preferably occurs in the tropical large-scale ascending zone (**Fig. 5d**), where cirrus formation is strongly connected to dehydrations associated with local wave activities. The January pattern of total TTL cirrus bears the classic Gill-model distribution in response to a heat forcing in the western Pacific [*Gill*, 1980]. The most frequent occurrence of cirrus does not collocate exactly with the location of the most frequent occurrence of deep convective centers (OLR<220 W/m^2, **Fig. 5d** white contour)

287 [e.g., *Massie et al.*, 2002; *Dessler et al.*, 2006; *Liu*, 2007], implying that cirrus is controlled
288 to the first order by planetary-scale wave dynamics and temperature variations instead of
289 individual convective centers [*Virts et al.*, 2010]. Over the Pacific, laminar cirrus occurs
290 more frequently towards the east, supporting the findings that the eastward-propagating
291 Kelvin waves play a significant role in thin cirrus formation [*Randel and Wu*, 2005; *Virts*
292 *et al.*, 2010]. On the other hand, laminar cirrus above equatorial Africa and South America
293 shifts westward, indicating a possible influence from the Rossby and gravity waves [*Boehm*
294 *and Lee*, 2003]. The total diabatic heating rates from MERRA2 shows that the tropical
295 laminar cirrus is frequently located at the broad, planetary-scale upwelling zone where air
296 tends to ascend diabatically. This connection to the diabatic ascent zone has an important
297 implication for long-lived laminar cirrus and their influence on the stratospheric H_2O since
298 these thin cirri have a greater potential of contributing to the upper TTL total H_2O budget
299 after experiencing multiple lifecycles of the sublimation-deposition processes (Section 4).
300 The time-varying occurrence frequency of laminar cirrus derived from the auto-
301 selection method reveals further insights on the cloud's responses to temperatures.
302 Seasonal variation of tropopause clouds is strongly anti-correlated to the seasonality of
303 tropopause temperature (**Fig. 6**), and the latter is inversely connected to the strength of
304 upwelling regulated by the wave-forced Brewer-Dobson circulation [*Yulaeva et al*, 1994].
305 Therefore, more (less) frequent occurrence of cirrus results from the stronger (weaker)
306 upwelling that accompanies colder (warmer) tropopause temperatures during boreal winter
307 (summer) [*Wang et al.*, 1996; *Fu*, 2013]. As a subset of total cirrus, laminar cirrus shows
308 similar seasonality.

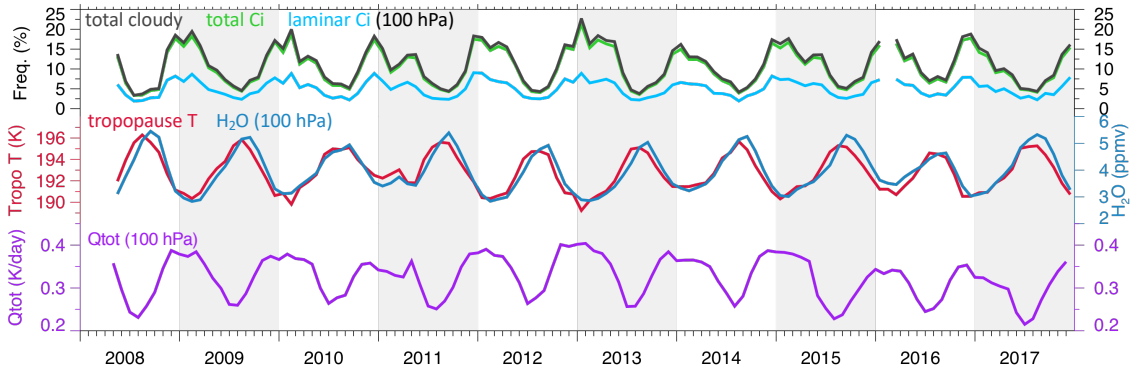

Figure 6. Seasonal variations of the 100-hPa totally cloudy (black), total cirrus (green), and laminar cirrus (light blue), comparing to the tropopause temperature (red), the MLS 100-hPa H_2O (deep blue), and the MERRA2 100-hPa total diabatic heating rates (purple, representing the strength of upwelling). Laminar cirrus is from auto-selection method, and all data are for the tropical 20° N–S average. There are no CALIPSO data on February 2016.

309

310 The temperature-cirrus anticorrelation is also robust at interannual scale. To better
311 understand the variability of laminar cirrus to temperatures, we perform a multivariate
312 linear regression analysis of the tropopause level (100-hPa) laminar cirrus frequency
313 against the following three terms that are directly related to the variability of tropopause
314 temperature:

315 $$CF_{cirrus} = a\,\Delta T + b\,QBO + c\,BDC + \varepsilon \qquad (2)$$

316 This regression model is similar to the one used in *Dessler et al* [2013] and *Ye et*
317 *al.*, [2017]. Here, ΔT is the tropical average 500-hPa temperature anomaly in Kelvin, which
318 is superior to the ENSO index because it captures more subtle variability of clouds (see
319 **Fig. 7a**). QBO is the quasi-biennial oscillation index based on NCEP/NCAR reanalysis of
320 30-hPa zonal wind (u30) at the equator from NOAA
321 (https://www.esrl.noaa.gov/psd/data/correlation/qbo.data), with positive/negative u30
322 denote westerly/easterly QBO phases. BDC is the Brewer-Dobson Circulation index
323 derived from the 100-hPa MERRA2 diabatic heating anomaly averaged over tropical 20°
324 N–S, with positive/negative values suggesting anomalously stronger/weaker upwelling.
325 The last term ε is the residual. There are physical mechanisms by which QBO and BDC

may be correlated, but the correlation is not statistically significant for this analyzing period (r = –0.37). To maximize the explained variance and also account for time it takes for regressors to impact the tropopause level clouds, we lag ΔT by 1 month and lag QBO index by 5 months. There is no lag in BDC index. While regressing, we also standardized all indices by dividing their own standard deviation. At the tropopause, cirrus frequency and cirrus IWC are highly correlated [*Flury et al.*, 2012], therefore, the analysis here also applies to laminar cirrus IWC.

Fig. 7 shows that the regression does a fairly good job in reproducing the variability of laminar cirrus observed by the CALIOP. The regression is able to explain total 46% of variance for 2008-2017 (panel d). The coefficients for ΔT, QBO, and BDC are 0.54, -0.4, and 0.76, respectively, indicating overall in-phase response of cirrus to the ΔT and the BDC, and out-of-phase response of cirrus to the QBO (**Fig. 7a-c**). Specifically, warming in the upper troposphere (+ΔT) during El Nino years cools the tropopause [e.g., *Garfinkel et al.*, 2013] and favors cirrus formation; similarly, stronger upwelling (+BDC index) cools the tropopause and enhances formation of cirrus in constantly saturated air [*Davis et al.*, 2013], resulting in more depletion of ambient H_2O; moreover, descending westerly shear of QBO (+QBO index) – with westerlies aloft and easterlies below, induces adiabatically warmed perturbation [*Plumb and Bell*, 1982] that reduces cirrus formation.

Ultimately, the interannual variability of the tropopause laminar cirrus is complicated by the interrelationships among the three factors. When ENSO's contribution is small, a stronger upwelling (+BDC index) during easterly shear of QBO (–QBO index) produces the most enhanced laminar cirrus (wintertime 2012-2013), while a weaker upwelling during westerly QBO yields the most reduced laminar cirrus (springtime 2017). During La Niña years when the colder upper troposphere (and then warmer tropopause) is

in phase with the warmly-perturbated westerly shear of QBO and the slightly weakened upwelling, laminar cirrus reduction is the most intense (December 2010 to May 2011).

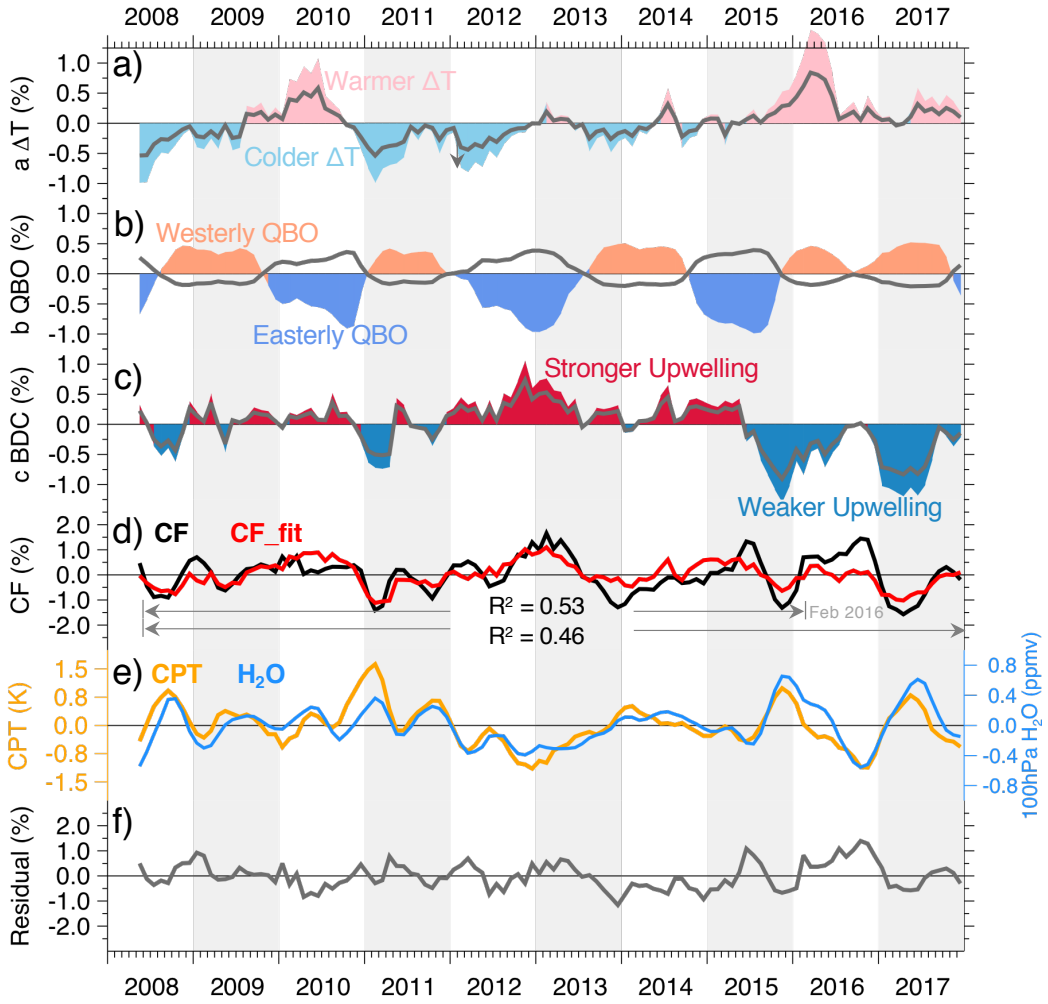

Figure 7. Components of the multivariant least-squares regression of laminar cirrus occurrence frequencies (CF) observed by the CALIOP. (a-c) Components of CF anomaly (dark gray lines, %) due to each individual regressors (color shading): (a) ΔT at 500 hPa, (b) Quasi-Biennial Oscillation (QBO), and (c) upwelling Brewer-Dobson circulation (BDC); (d) regressed CF (red) comparing to observed CF (black); (e) cold-point temperature anomaly (orange) and 100-hPa H_2O anomaly (blue); (f) the residual. The CTP and H_2O anomalies in panel e) are to demonstrate the overall regulation of temperatures to H_2O and to cirrus ice.

We also notice that the BDC (**Fig. 7c** shading) largely resembles the observed variability of laminar cirrus (**Fig. 7d** black curve, r=0.76), implying that the wave-driven upwelling anomaly plays a key role in modulating cirrus variability: a stronger upwelling is always accompanied by colder temperatures, increased cirrus frequencies, and decreased

H_2O; and vice versa. This temperature-H_2O-ice regulation is better shown when comparing to panel e the anomalies of cold-point tropopause and H_2O (100-hPa). Take the September–December 2015 for example: the anomalously weaker upwelling induces anomalously warmer tropopause, causing cirrus reduction when the strongly developing El Niño could have produced more cirrus in the tropopause. **Fig. 8** demonstrates that there is overall decreased cirrus and increased H_2O during the unusual El Niño of 2015-2016. During which, the enhanced center of laminar cirrus accompanies reduced H_2O, migrating from the western to the central Pacific, and it is speculated that this unusual El Niño causes more over-shooting deep convection that moistens the lower stratosphere [*Avery et al.*, 2017].

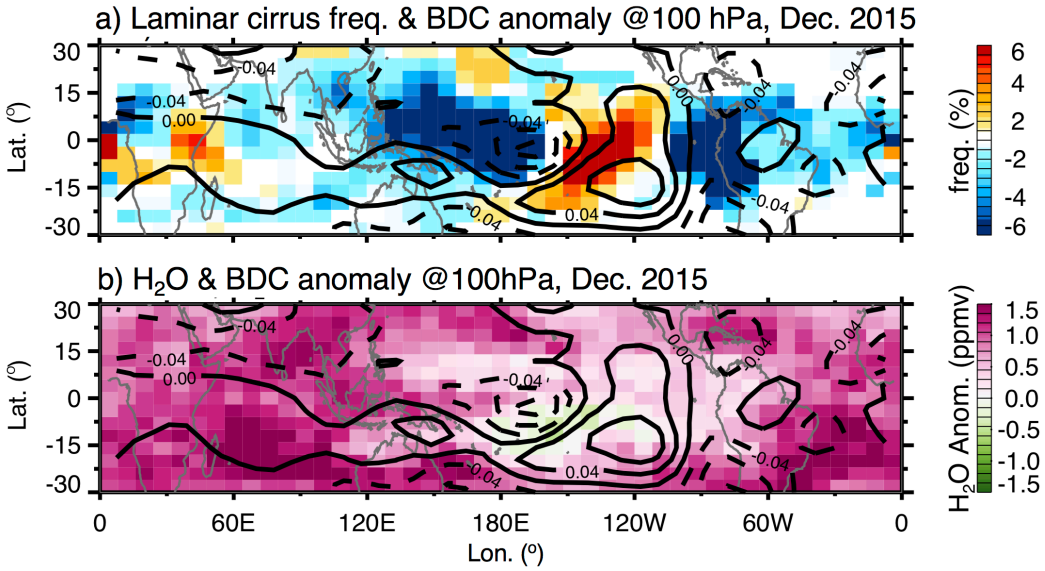

Figure 8. The anomalous 100 hPa (a) laminar cirrus and (b) H_2O in December 2015, overlaid by total diabatic heating rates anomaly (line contours, K/day) to highlight the dominant role of BDC to the variation of clouds.

Overall, the regression residual (**Fig. 7e**) is relatively small during most of the time. One exception is the year of 2015-2016 when the strong and unusual El Niño accompanies unprecedented disruption of the QBO [*Newman et al.*, 2016; *Osprey et al.*, 2016] that complicates the performance of the regression. Since 2015, cirrus frequency has experienced a change of 3.5% but our regression model only captures ~2%. Meanwhile,

the H_2O has experienced substantial change of ~1.3 ppmv, following the weakened upwelling precisely just as the strengthened upwelling did for the H_2O-drop in 2001 [*Randel et al.*, 2006]. The decrease in H_2O is somewhat complex due to the meddling of disrupted QBO. This suggests that other processes modulating the tropopause laminar cirrus may not be included and it is worth investigating in future work. If we exclude the period after February 2016, the explained variance increases to 53%.

3.2. Laminar cirrus ice amount

The frequent occurrence and long lifetime of laminar cirrus highlight the need for quantifying the amount of cloud ice that interchanges with H_2O in the TTL. We use the IWC provided in the CALIOP MLay product, granted that there may exist a scaling error of 50-100% [*Wu et al*, 2009, 2014]. However, such a scaling error does not affect the results of derived cirrus-H_2O correlation but carrying the same scaling uncertainty in the derived cirrus contribution to the total H_2O budget. Nevertheless, the CALIOP IWC is one of the best products that are available for evaluating cirrus ice in the TTL.

To quantify the relation between laminar cirrus ice and ambient H_2O, we calculate the ice amount laminar cirrus carries. Take the 100-hPa as an example, we chose a vertical range between 110-90 hPa, then the ice water content (IWC) – by definition the ice amount per unit volume, is calculated as

$$IWC = \frac{total\ ice\ amount}{total\ observing\ volume} = \frac{\sum_{j=1}^{mCld} pIWP_j \times A_j}{\sum_{i=1}^{nObs} layH_i \times A_i} = \frac{\sum_{j=1}^{mCld} pIWP_j}{\sum_{i=1}^{nObs} layH_i} \quad (3)$$

Here, *pIWP* is the partial ice water path integrated for each layer of laminar cirrus within the vertical range, in g/m^2; *layH* is the layer thickness in meter; *A* is the profile area with 5-km along track and 70-m across track [*Winker et al.*, 2003]. The IWC is then expressed as the total ice amount of *m* cirrus layers divided by the total observing volume of *n*

observations. Generally, $m<n$. With area A constant for each profile, IWC is effectively the ratio of total *pIWP* for m cirrus to total *layH* for n observations. For easy comparison with the MLS H_2O, we convert IWC to volume mixing ratio (*ppmv*) via ideal gas law. That means, at 100 hPa with typical temperature of 191 K, IWC in 1 mg/m^3 approximately equals to 8.8 *ppmv* gas equivalent.

Most of laminar cirrus is found to have low IWC, high H_2O, located in supersaturated air. Take the clouds in January 2009 as an example, **Fig. 9** shows the joint histograms of manually selected laminar cirrus IWC vs. H_2O as a function of cirrus occurrence frequency (panel a) and RHi (panel b). Laminar cirrus occurs most frequently in saturated or supersaturated conditions, where H_2O is between 2-4 ppmv and IWC is < 1 ppmv. This is in general agreement with what the Global Hawk observed of cirrus layers frequently situated in supersaturated air [*Jensen et al.*, 2013].

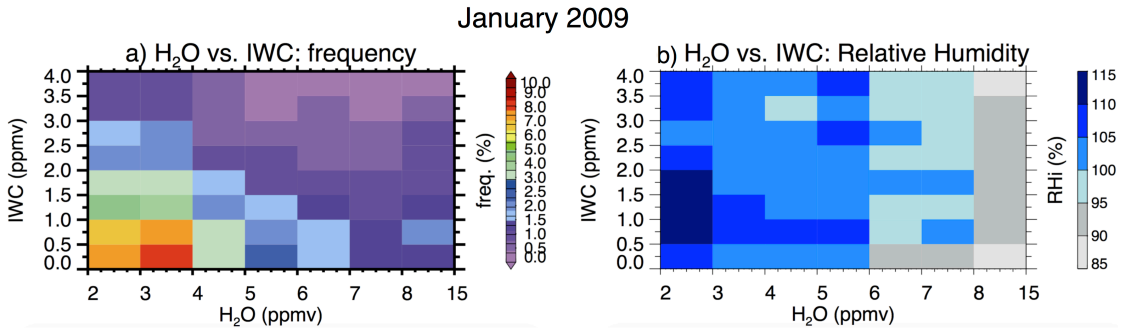

Figure 9. Joint histograms of laminar cirrus H_2O vs. IWC (both in ppmv) in function of a) occurring frequency and b) relative humidity with respect to ice (RHi) for January 2009. The results are from manual-selection of laminar cirrus.

Laminar cirrus ice amount also shows clear annual cycle, with strong dependence on the tropopause temperature and therefore the relative humidity and the ambient H_2O abundances. **Fig. 10a** shows the zonal mean time series of 100-hPa laminar cirrus IWC, superimposed with ambient H_2O (black contours) and RHi (grey contours). Obviously, IWC and H_2O show seasonal cycle but in out-of-phase sequences: higher IWC accompanies lower H_2O during boreal winter when colder air favors nucleation in

(super)saturated environment; during boreal summer it is the opposite. It implies that TTL H_2O is a direct response to tropopause temperature via dehydration of air sourced from below; meanwhile the TTL laminar cirrus is also a direct response to tropopause temperature via nucleation of available H_2O sourced from ambient air.

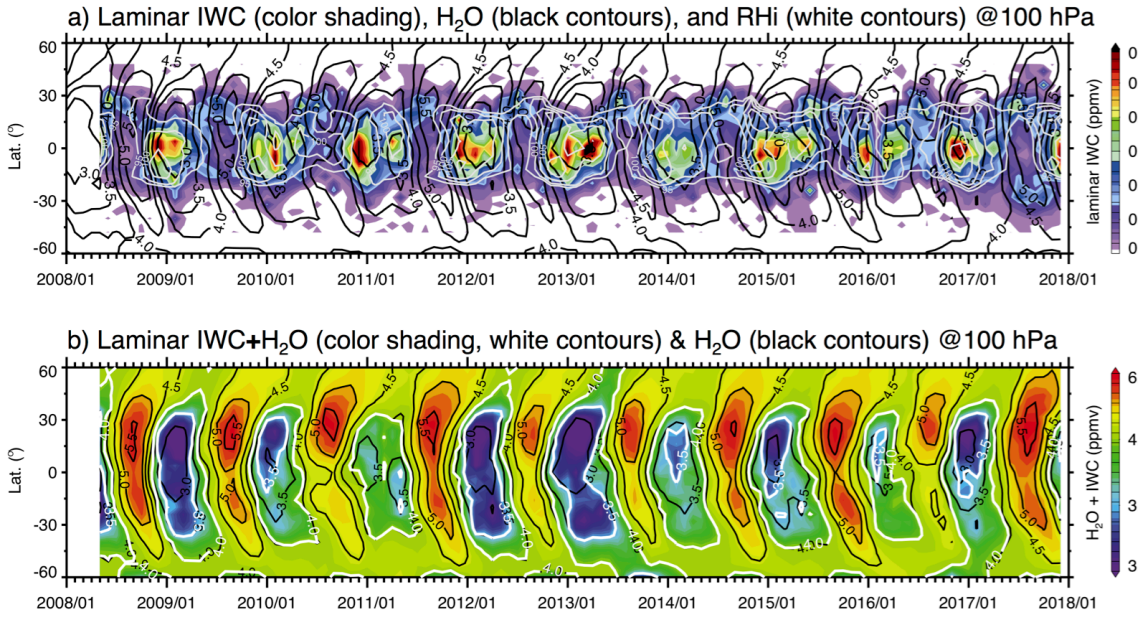

Figure 10. Evolution of zonal mean a) laminar cirrus IWC (color shading), H_2O (black contours), and RHi (white contours); and b) total water IWC+H_2O (color shading) and H_2O (black contours) at 100 hPa for the period of 2008-2017. In both panels the black contours repeat for H_2O in ppmv. In panel b) the total water (IWC+H_2O) in 3.5 and 4.0 ppmv are highlighted in thick, white contours.

Unlike H_2O, laminar cirrus IWC does not show poleward transport by the meridional overturning Brewer-Dobson circulation because the cirrus ice is subject to loss processes through sedimentation and sublimation. In the tropics during boreal winter, laminar cirrus frequently carries 0.4-0.6 ppmv of ice while ambient H_2O is between 3-3.5 ppmv. If we add ice water to ambient vapor vapor, **Fig. 10b** shows that the ambient total available water (IWC+H_2O) will likely to be homogenized and relaxed to 3.5-4 ppmv (thick white contours). During boreal summer, there is no change in total available water if we add ice since the laminar ice is so less.

Interannually, the variability of tropical cirrus IWC – similar to that of cirrus

429 frequency, is also anti-correlated to the variability of tropical H_2O, implying a strong
430 modulation between H_2O and ice by the temperatures. This relation is dominated by the
431 regions of most frequent laminar cirrus (comparing **Fig. 11a** to **Fig. 5a**), where air RHi is
432 frequently higher than 100% (black contours in **Fig. 11a**). To quantify this interannually
433 varying IWC-H_2O regulation, we perform linear regression of gridded IWC and H_2O
434 monthly anomalies with the relation $\Delta IWC = a^* \Delta H_2O + b$, with enhanced negative slope
435 indicating anomalously more depletion of H_2O into laminar cirrus ice. Shown in **Fig. 11b,**
436 regions of enhanced negative slopes are exactly the regions of the most frequent laminar
437 cirrus, where 1 ppmv decrease in H_2O corresponds to 0.2-0.3 ppmv increase in cirrus IWC.
438 Our regional relation map differs from previous studies in that we only examined
439 laminar cirrus occurring *in situ*, whereas previous studies focused on total cirrus including
440 the thick ones closely tied to deep convective anvils. Therefore, in previous studies the
441 regions of anti-correlation largely overlap with convection centers including the Asian
442 monsoon sector [e.g., *Flury et al.*, 2012]. Over the Tibetan Plateau and the south tip of
443 South America, where the 100-hPa level is generally below the local tropopause (**Fig. 11c**
444 color shading) by 200-600 meters (**Fig. 11c** white contours), laminar cirrus ice anomaly
445 shows a positive response to H_2O anomaly, due to relatively abundant supply of H_2O from
446 the below air. This also implies that finer vertical resolution resolving vertical gradients of
447 H_2O around the tropopause is necessary for precise study of cirrus' effect on the
448 dehydration/hydration of air in the TTL.

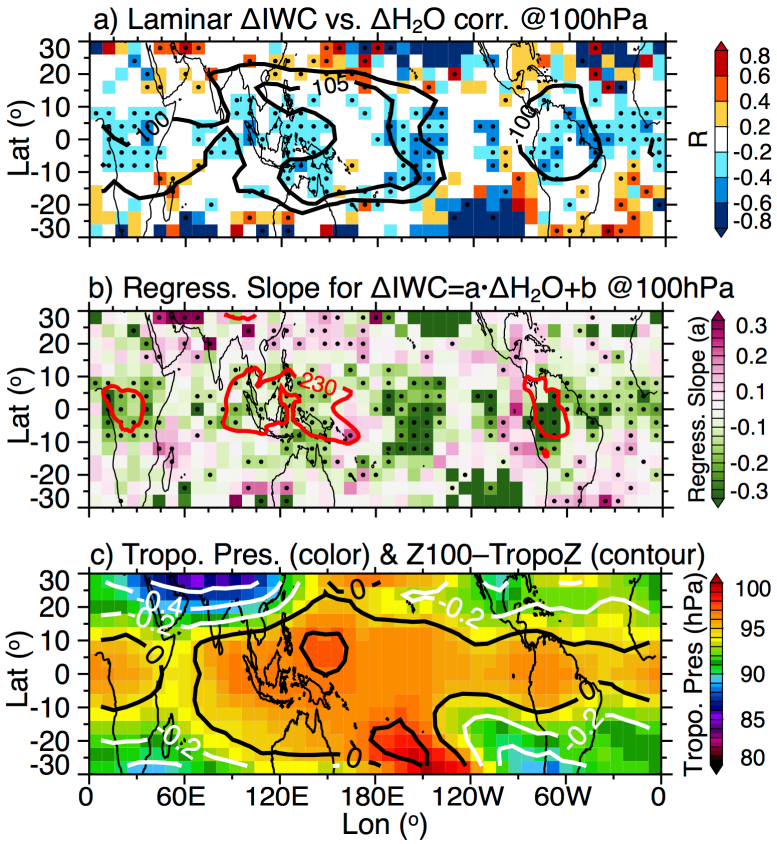

Figure 11. a) Correlation coefficients between IWC anomaly (ΔIWC) and H_2O anomaly (ΔH_2O) for laminar cirrus at 100 hPa for 2008-2017, with RHi (super)saturation contoured in black lines; b) linear regression slope for anomalous IWC in response to anomalous H_2O with relation $\Delta IWC = a \bullet \Delta H_2O + b$ at 100 hPa, overlaid with CERES average OLR < 230 W/m^2 in red contours indicating regions of the most frequent deep convection; c) cold-point tropopause mean pressure (color shading) for 2008-2017, with differences of 100-hPa height to the cold-point tropopause height contoured (0.2 km interval, negative in white and positive in black). In panels a-b the ΔH_2O and ΔIWC are calculated by removing the annual cycle of each during 2008-2017, and the black dots indicate the relation significantly greater than 95% confidence level.

4. Discussion

Given the frequently higher relative humidity with respect to ice at the tropopause (**Figs. 9b, 10a, 11a**), we expect laminar cirrus to sustain long in the TTL [*Winker and Trepte*, 1998; *Garrett et al.*, 2004; *Dinh* et al., 2010; *Taylor et al.*, 2011]. During this long lifetime, cloud-induced radiative heating is able to further maintain the cloud itself [*Lilly*, 1998; *Dinh* et al., 2010]. Under this scenario we speculate that laminar cirrus effectively interchanges mass with H_2O and travel together with H_2O over multiple phase-change

457 lifecycles to eventually affect the total H_2O budget at upper levels. This indicates that
458 laminar cirrus could exist as one of the important reservoirs for water storage.

459 **Fig. 12** supports the hypothesis that laminar cirrus at the 100 hPa can contribute
460 significantly to the lower stratosphere total H_2O. **Fig. 12a** shows the climatology of H_2O
461 tape recorder – an upward advection of successive minima and maxima in H_2O retained
462 from the tropopause [*Mote et al*., 1996]. Specifically, during the dry season (December-
463 February) the low H_2O imprinted at the 100 hPa (the tropopause) gets *enhanced* (wetter)
464 at 68 hPa (top of TTL at ~19 km, *Fueglistaler et al.*, [2009]), while during the wet season
465 (June-August) the high H_2O imprinted at the tropopause gets slightly *diluted* (drier) while
466 travelling upward. This results in overall smaller magnitude of H_2O annual cycle at the 68
467 hPa (**Fig. 12b**). That said, following the start of the tape recorder signal imprinted at the
468 tropopause, there is an overall positive/negative vertical gradient following the tape starting
469 from the dry/wet tongue (**Fig. 12b**). Previous analysis argued that this positive vertical
470 gradient along the vertical propagation of dry tongue is due to mixing of aged, H_2O-rich
471 air (*Mote* et al., [1996]) descending from the upper stratosphere where methane oxidation
472 becomes important (*Dessler et al.*, [1994]).

473 However, we intend to limit our analysis to the deep tropics (12^o N–S) where
474 mixing at this altitude is much weaker. Especially, when we limit the analysis to the tropical
475 Western Pacific (120-180^{o}E) where mixing is the least important, the positive vertical
476 gradient following the dry tongue is even greater. This argues another plausible explanation
477 for the positive vertical gradient following the dry tongue: the laminar cirrus ice formed at
478 100 hPa might eventually contribute to the addition of H_2O at 68 hPa via sublimation of
479 ice particles into vapor (**Fig. 12c-d**). Here, the TTL laminar cirrus acts as a reservoir of

480 water storage that it might interchanges mass with vapor over multiple lifecycles of
481 sublimation-deposition before ascending to higher levels.

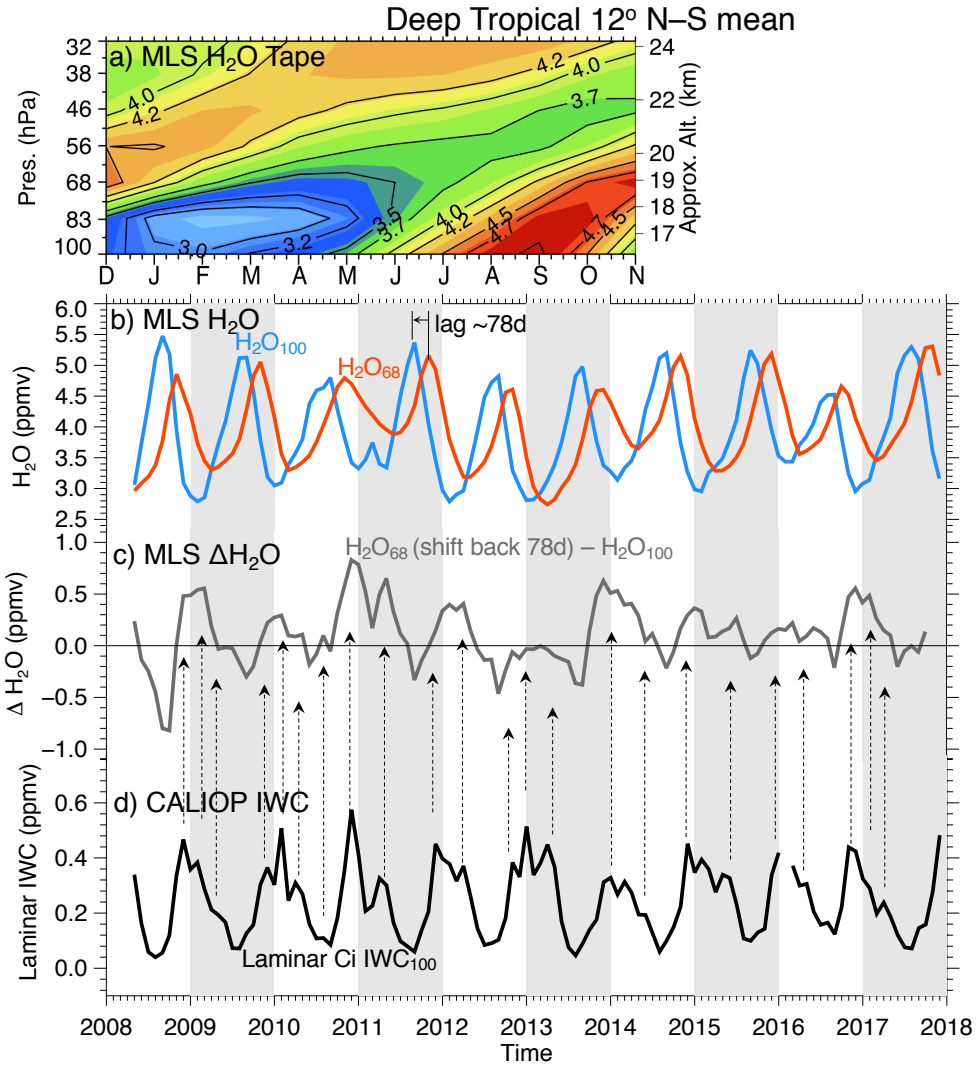

Figure 12. MLS observed tropical (12° N–S) a) H_2O tape recorder climatology; b) H_2O time series at 100 hPa (H_2O_{100}, blue) and 68 hPa (H_2O_{68}, orange red); c) the difference between H_2O_{68} shifted for 78 days and H_2O_{100} ($H_2O_{68shift} - H_2O_{100}$); d) the CALIOP laminar cirrus IWC at 100 hPa (IWC_{100}).

482

483 However, the exact amount of ice eventually contributing to the total water budget
484 at 68-hPa is not easy to quantify since there is no accurate way to isolate the effect from
485 mixing completely. Therefore, we speculate that up to 10% of total H_2O abundances in
486 upper levels could be attributable to lower-level laminar cirrus ice in the deep tropics (i.e.,

~0.5 ppmv of IWC at 100 hPa over ~5 ppmv of H_2O at 68 hPa). This implies that the laminar cirrus at the tropopause might have a hydrating effect on the lower stratosphere.

5. Conclusion Remarks

A laminar cirrus database is obtained by manually selecting the isolated, extensive layers of enhanced CALIOP Level-1 532nm total attenuated backscatter for January 2009. The characteristics of the selected laminar cirrus are used to develop an automatic selection algorithm, so as to pick up the similar class of laminar cirrus from a 10-year (2008-2017) CALIOP Level-2 merged layer product. This enables us to study the laminar cirrus and its relation to the TTL water vapor in a much longer time scale.

The laminar cirrus database shows that most laminar cirrus has a cloud base at 15-17 km, thickness of 0.5-1 km, optical depth (τ) less than 0.03, and partial ice water path (pIWP) less than 0.3 g/m^2 (**Figs. 2-3**). They often occur in a location away from deep convective centers, where saturation is subject more to temperature modulation than to convection (**Figs. 4-5, 11**).

Laminar cirrus contributes at least 30-40% to the total cirrus population in terms of occurrence frequency near the tropopause (**Fig. 2**). The annual variation of laminar cirrus follows that of total cirrus closely (**Figs. 6**), with preferable appearance in boreal winter [e.g., *Massie et al*., 2002; *Wang et al.*, 2012] when the tropopause is colder (**Figs. 5, 10**) and in constant (super)saturation (**Figs. 9-11**).

Tropopause temperature plays a key role in controlling the total water budget and the partition between the H_2O and cirrus ice amount on both seasonal (**Figs. 6, 10**) and interannual scales (**Figs. 7, 11**). On the seasonal scale, a higher and colder tropopause leads to more frequent (super)saturation during boreal winter, favors more efficient dehydration

511 that depletes H_2O and enhances laminar cirrus frequency and IWC. In wintertime, laminar
512 cirrus has a total of 0.4-0.6 ppmv IWC situated in a 3-3.5 ppmv H_2O background, i.e., the
513 total available water (IWC+H_2O) is relaxed to total ~3.5-4 ppmv. During boreal summer,
514 a warmer, often undersaturated tropopause leads to fewer formation of laminar cirrus
515 despite more H_2O supply from the below. The overall tropopause laminar cirrus frequency
516 and ice amount are highly correlated. The anti-correlation between the tropopause H_2O and
517 laminar cirrus suggests a significant amount of water storage in cirrus as part of the total
518 water budget.

519 Interannually, the variability of tropopause laminar cirrus is attributable to the
520 variations of the troposphere temperature (ΔT), the quasi-biennial oscillation (QBO), and
521 the upwelling branch of the Brewer-Dobson circulation (BDC). The interrelationships of
522 among these processes have direct impact on the tropopause temperatures such that
523 anomalously warmer ΔT, easterly shear of QBO, and stronger upwelling all cool the
524 tropopause and then enhance cirrus formation. Specifically, the wave-driven upwelling
525 (BDC) seems to play a dominating role in laminar cirrus formation – similar as BDC to
526 lower stratospheric H_2O [*Dessler et al.*, 2013, 2014]. It is expected that the variability of
527 laminar cirrus is immediately anti-correlated to that of H_2O, and this study provides a more
528 quantitative estimate of such anticorrelation. In regions of the most frequent laminar cirrus,
529 a 1 ppmv decrease in H_2O corresponds to 0.2-0.3 ppmv increase in cirrus IWC. In summary,
530 the TTL H_2O is a direct response to the tropopause temperature via *dehydration of air*
531 ***sourced from below***; whereas TTL laminar cirrus is a direct response to the tropopause
532 temperature via *nucleation of available H_2O* ***sourced from ambient air***.

533 Laminar cirrus might contribute to the TTL water and radiation budget over its
534 relatively long lifetime [e.g., *Jensen et al.*, 1996; *Garrett et al.*, 2004; *Dinh et al.*, 2010;

Taylor et al., 2011]. Frequently situated in (super)saturated air, small ice mass and small particles are likely to allow laminar cirrus to survive multiple sublimation-deposition lifecycles in the TTL. Tropical laminar cirrus is frequently located at the enhanced upwelling zone where air tends to ascend diabatically. As illustrated in **Fig. 13**, thin, tenuous laminar cirrus layers with a sufficient long lifetime could interchange with H_2O and eventually become stratospheric H_2O. It is found that the H_2O gain at 68 hPa (19 km) could be directly related to sublimation of the laminar cirrus ice imprinted at the tropopause 100-hPa. The addition of H_2O at 68 hPa suggests that the laminar ice might contribute up to 10% to the total H_2O entering the stratosphere, a hydrating effect to the stratosphere. This is the hydrating effect due to underestimating of total water when the laminar cirrus ice is not visible to the MLS. Note that this hydrating effect is different from those caused by the convectively lofted ice in current [*Ye et al.*, 2018] and future climate [*Dessler et al.*, 2016].

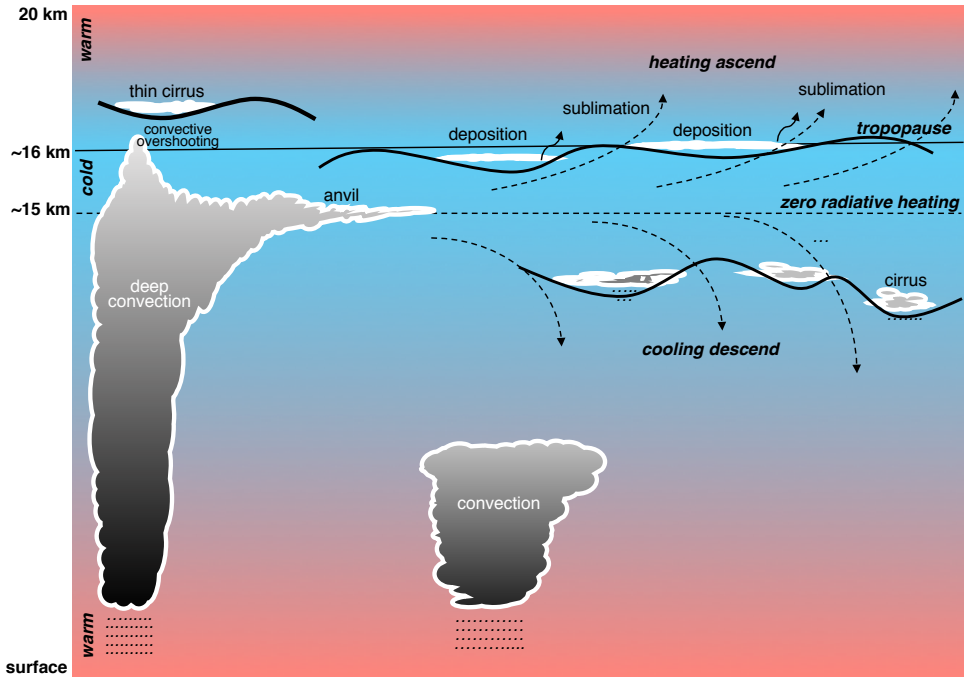

Figure 13. Schematic formation and transport of laminar cirrus, thin cirrus, and convective clouds in the TTL environment. Thin and laminar cirrus mostly forms at the cold phases of tropical waves (wavy lines) and may survive multiple warm-cold cycles as a significant contributor to the total water budget near the tropopause. During sublimation/deposition exchanges with water vapor, some may rise into the stratosphere and some may precipitate out. The thick solid line denotes the tropopause, and straight, dashed line is the level of zero radiative heating.

549

550

551

552 **Acknowledgements**

553

554 The CALIOP data is publicly available from the NASA Earth Data Atmospheric Science
555 Data Center (ASDC) at https://eosweb.larc.nasa.gov/. The MLS and MERRA2 data are
556 available at the NASA Earth Data Goddard Earth Science (GES) Data and Information
557 Services Center (DISC). This work is supported by NASA Atmospheric Composition
558 Modeling and Analysis Program (ACMAP), with project NNH16ZDA001N-ACMAP. We
559 thank comments from Eric Jensen (NASA AMES) and from Mark Schoeberl and John
560 Kummer (Science and Technology Corporation).

References

Avery, M. A., Davis, S., Rosenlof, K., Ye, H., & Dessler, A. E. (2017). Large anomalies in lower stratospheric water vapour and ice during the 2015–2016 El Niño. Nature Geoscience, 10(6), 405–409. https://doi.org/10.1038/NGEO2961

Boehm, M. T., and J. Verlinde (2000), Stratospheric influence on upper tropospheric tropical cirrus, Geophys. Res. Lett., 27(19), 3209–3212, doi: 10.1029/2000GL011678.

Boehm, M.T. and S. Lee (2003): The Implications of Tropical Rossby Waves for Tropical Tropopause Cirrus Formation and for the Equatorial Upwelling of the Brewer–Dobson Circulation. J. Atmos. Sci., 60, 247–261, https://doi.org/10.1175/1520-0469(2003)060<0247:TIOTRW>2.0.CO;2

Corti, T., Luo, B. P., Fu, Q., Vömel, H., and Peter, T. (2006): The impact of cirrus clouds on tropical troposphere-to-stratosphere transport, Atmos. Chem. Phys., 6, 2539-2547, https://doi.org/10.5194/acp-6-2539-2006.

Davis, S. M., C. K. Liang, and K. H. Rosenlof (2013), Interannual variability of tropical tropopause layer clouds, Geophys. Res. Lett., 40, 2862–2866, doi:10.1002/grl.50512.

Danielsen, E. F. (1993), In situ evidence of rapid, vertical, irreversible transport of lower tropospheric air into the lower tropical stratosphere by convective cloud turrets and by larger-scale upwelling in tropical cyclones, J. Geophys. Res., 98(D5), 8665–8681, doi:10.1029/92JD02954.

Dessler, A. E., Weinstock, E. M., Hintsa, E. J., Anderson, J. G., Webster, C. R., May, R. D., Elkins, J. W., and Dutton, G. S. (1994), An examination of the total hydrogen budget of the lower stratosphere, Geophys. Res. Lett., 21, 2563–2566.

Dessler, A. E., S. P. Palm, W. D. Hart, and J. D. Spinhirne (2006), Tropopause-level thin cirrus coverage revealed by ICESat/Geoscience Laser Altimeter System, J. Geophys. Res., 111, D08203, doi:10.1029/2005JD006586.

Dessler, A. E., M. R. Schoeberl, T. Wang, S. M. Davis, and K. H. Rosenlof (2013), Stratospheric water vapor feedback, Proc. Natl. Acad. Sci. U.S.A., 110, 18,087–18,091, doi:10.1073/pnas.1310344110.

Dessler, A. E., M. R. Schoeberl, T. Wang, S. M. Davis, K. H. Rosenlof, and J.-P. Vernier (2014), Variations of stratospheric water vapor over the past three decades, J. Geophys. Res. Atmos., 119, 12,588–12,598, doi:10.1002/2014JD021712.

Dessler, A.E., H. Ye, T. Wang, M.R. Schoeberl, L.D. Oman, A.R. Douglass, A.H. Butler, K.H. Rosenlof, S.M. Davis, and R.W. Portmann (2016), Transport of ice into the stratosphere and the humidification of the stratosphere over the 21st century, Geophys. Res. Lett., 43, doi: 10.1002/2016GL067991, 2323-2329.

Dinh, T. P., D. R. Durran, and T. P. Ackerman (2010), Maintenance of tropical tropopause layer cirrus, J. Geophys. Res., 115, D02104, doi:10.1029/2009JD012735.

Flury, T., Wu, D. L., and Read, W. G. (2012), Correlation among cirrus ice content, water vapor and temperature in the TTL as observed by CALIPSO and Aura/MLS, Atmos. Chem. Phys., 12, 683-691, https://doi.org/10.5194/acp-12-683-2012.

Fu, Q. (2013): Bottom up in the tropics. Nature Clim. Change, 3, 957 - 958, doi:10.1038/nclimate2039.

Fueglistaler, S., Dessler, A. E., Dunkerton, T. J., Folkins, I., Fu, Q., and Mote, P. W. (2009), The tropical tropopause layer, Rev. Geophys., 47, RG1004, doi:10.1029/2008RG000267.

Gage, K. S., and G. C. Reid (1987), Longitudinal variations in tropical tropopause properties in relation to tropical convection and El Niño-Southern Oscillation events, J. Geophys. Res., 92(C13), 14197–14203, doi: 10.1029/JC092iC13p14197.

Garfinkel, C. I., D. W. Waugh, L. D. Oman, L. Wang, and M. M. Hurwitz (2013), Temperature trends in the tropical upper troposphere and lower stratosphere: Connections with sea surface temperatures and implications for water vapor and ozone, J. Geophys. Res. Atmos., 118, 9658–9672, doi:10.1002/jgrd.50772.

Garrett, T. J., A. J. Heymsfield, M. J. McGill, B. A. Ridley, D. G. Baumgardner, T. P. Bui, and C. R. Webster (2004), Convective generation of cirrus near the tropopause, J. Geophys. Res., 109, D21203, doi:10.1029/2004JD004952.

Gelaro, R., W. McCarty, M.J. Suárez, R. Todling, A. Molod, L. Takacs, C.A. Randles, A. Darmenov, M.G. Bosilovich, R. Reichle, K. Wargan, L. Coy, R. Cullather, C. Draper, S. Akella, V. Buchard, A. Conaty, A.M. da Silva, W. Gu, G. Kim, R. Koster, R. Lucchesi, D. Merkova, J.E. Nielsen, G. Partyka, S. Pawson, W. Putman, M. Rienecker, S.D. Schubert, M. Sienkiewicz, and B. Zhao (2017): The Modern-Era Retrospective Analysis for Research and Applications, Version 2 (MERRA-2). J. Climate, 30, 5419–5454, https://doi.org/10.1175/JCLI-D-16-0758.1

618 Gill, A. (1980). Some simple solutions for heat-induced tropical circulation. Quarterly Journal of the Royal
619 Meteorological Society, 106(449), 447–462.
620 Heymsfield, A., D. Winker, M. Avery, M. Vaughan, G. Diskin, M. Deng, V. Mitev, and R. Matthey, 2014:
621 Relationships between Ice Water Content and Volume Extinction Coefficient from In Situ
622 Observations for Temperatures from 0° to −86°C: Implications for Spaceborne Lidar Retrievals. J.
623 Appl. Meteor. Climatol., 53, 479–505, https://doi.org/10.1175/JAMC-D-13-087.1
624 Immler, F., K. Krüger, M. Fujiwara, G. Verver, M. Rex, and O. Schrems (2008), Correlation between
625 equatorial Kelvin waves and the occurrence of extremely thin ice clouds at the tropical tropopause,
626 Atmos. Chem. Phys., 8, 4019–4026, doi:10.5194/acp-8-4019-2008.
627 Jensen, E. J., O. B. Toon, H. B. Selkirk, J. D. Spinhirne, and M. R. Schoeberl (1996), On the formation and
628 persistence of subvisible cirrus clouds near the tropical tropopause, J. Geophys. Res., 101(D16),
629 21361–21375, doi: 10.1029/95JD03575.
630 Jensen, E. J., et al. (1998), Ice nucleation processes in upper tropospheric wave-clouds observed during
631 SUCCESS, Geophys. Res. Lett., 25, 1363-1366.
632 Jensen, E., and Pfister, L. (2004): Transport and freeze-drying in the tropical tropopause layer, J. Geophys.
633 Res., 109, D02207, doi:10.1029/2003JD004022.
634 Jensen, E. J., G. Diskin, R. P. Lawson, S. Lance, T. P. Bui, D. Hlavka, M. McGill, L. Pfister, O. B. Toon,
635 and R. Gao (2013), Ice nucleation and dehydration in the Tropical Tropopause Layer, Proc. Natl.
636 Acad. Sci. U.S.A., 110, 2041–2046, doi:10.1073/pnas.1217104110.
637 Kar, J., Vaughan, M. A., Lee, K.-P., Tackett, J. L., Avery, M. A., Garnier, A., Getzewich, B. J., Hunt, W. H.,
638 Josset, D., Liu, Z., Lucker, P. L., Magill, B., Omar, A. H., Pelon, J., Rogers, R. R., Toth, T. D., Trepte,
639 C. R., Vernier, J.-P., Winker, D. M., and Young, S. A. (2018): CALIPSO lidar calibration at 532 nm:
640 version 4 nighttime algorithm, Atmos. Meas. Tech., 11, 1459-1479, https://doi.org/10.5194/amt-11-
641 1459-2018.
642 Lambert, A., et al. (2007), Validation of the Aura Microwave Limb Sounder middle atmosphere water vapor
643 and nitrous oxide measurements, J. Geophys. Res., 112, D24S36, doi:10.1029/2007JD008724.
644 Lilly, D. (1988), Cirrus outflow dynamics, J. Atmos. Sci., 45, 1594–1605.
645 Liu, C. (2007), Geographical and seasonal distribution of tropical tropopause thin clouds and their relation
646 to deep convection and water vapor viewed from satellite measurements, J. Geophy s. Res.,
647 112,D09205,doi:10.1029/2006JD007479.
648 Liu, Z., Kar, J., Zeng, S., Tackett, J., Vaughan, M., Avery, M., Pelon, J., Getzewich, B., Lee, K.-P., Magill,
649 B., Omar, A., Lucker, P., Trepte, C., and Winker, D. (2019): Discriminating between clouds and
650 aerosols in the CALIOP version 4.1 data products, Atmos. Meas. Tech., 12, 703-734,
651 https://doi.org/10.5194/amt-12-703-2019.
652 Luo, B. P., Peter, Th., Wernli, H., Fueglistaler, S., Wirth, M., Kiemle, C., Flentje, H., Yushkov, V. A.,
653 Khattatov, V., Rudakov, V., Thomas, A., Borrmann, S., Toci, G., Mazzinghi, P., Beuermann, J.,
654 Schiller, C., Cairo, F., Di Don-Francesco, G., Adriani, A., Volk, C. M., Strom, J., Noone, K., Mitev,
655 V., MacKenzie, R. A., Carslaw, K. S., Trautmann, T., Santacesaria, V., and Stefanutti, L.: Ultrathin
656 Tropical Tropopause Clouds (UTTCs): II. Stabilization mechanisms, Atmos. Chem. Phys., 3, 1093-
657 1100, https://doi.org/10.5194/acp-3-1093-2003, 2003.
658 McGill, M. J., M. A. Vaughan, C. R. Trepte, W. D. Hart, D. L. Hlavka, D. M. Winker, and R. Kuehn (2007),
659 Airborne validation of spatial properties measured by the CALIPSO lidar, J. Geophys. Res., 112,
660 D20201, doi: 10.1029/2007JD008768.
661 McFarquhar, G., A. Heymsfield, J. Spinhirne, and B. Hart (2000), Thin and subvisual tropopause tropical
662 cirrus: Observations and radiative impacts, J. Atmos. Sci., 57, 1841–1853, doi:10.1175/1520-
663 0469(2000)057<1841: TASTTC>2.0.CO;2.
664 Marchant, B., Platnick, S., Meyer, K., Arnold, G. T., and Riedi, J. (2006): MODIS Collection 6 shortwave-
665 derived cloud phase classification algorithm and comparisons with CALIOP, Atmos. Meas. Tech., 9,
666 1587-1599, https://doi.org/10.5194/amt-9-1587-2016.
667 Martins, E., V. Noel, and H. Chepfer (2011), Properties of cirrus and subvisible cirrus from nighttime
668 Cloud-Aerosol Lidar with Orthogonal Polarization (CALIOP), related to atmospheric dynamics and
669 water vapor, J. Geophys. Res., 116, D02208, doi:10.1029/2010JD014519.
670 Massie, S., A. Gettelman, W. Randel, and D. Baumgardner (2002), Distribution of tropical cirrus in relation
671 to convection, J. Geophys. Res., 107(D21), 4591, doi:10.1029/2001JD001293.
672 Mote, P. W., K. H. Rosenlof, M. E. McIntyre, E. S. Carr, J. C. Gille, J. R. Holton, J. S. Kinnersley, H. C.
673 Pumphrey, J. M. Russell III, and J. W. Waters (1996), An atmospheric tape recorder: The imprint of
674 tropical tropopause temperatures on stratospheric water vapor, J. Geophys. Res., 101, 3989–4006,
675 doi:10.1029/95JD03422.

676 Newman, P. A., Coy, L., Pawson, S., and Lait, L. R. (2016), The anomalous change in the QBO in 2015–
677 2016, Geophys. Res. Lett., 43, 8791– 8797, doi:10.1002/2016GL070373.
678 Osprey, S., Butchart, N., Knight, J. R., Scaife, A. A., Hamilton, K., Anstey, J. A., … Zhang, C. (2016). An
679 unexpected disruption of the atmospheric quasi-biennial oscillation. Science, 353(6306), 1424– 1427.
680 Platt, C. M. R. (1973), Lidar and radiometric observations of cirrus clouds, J. Atmos. Sci., 30, 1191–1204.
681 Plumb, R. A., and R. C. Bell (1982), A model of the quasi-biennial oscillation on an equatorial beta-plane,
682 Q. J. Roy Meteor. Soc., 108(456), 335–352.
683 Pfister, L., et al. (2001), Aircraft observations of thin cirrus clouds near the tropical tropopause, J. Geophys.
684 Res., 106(D9), 9765–9786, doi: 10.1029/2000JD900648.
685 Potter, B. E., and J. R. Holton (1995), The role of monsoon convection in the dehydration of the lower
686 tropical stratosphere, J. Atmos. Sci., 52, 1034 – 1050.
687 Randel, W. J., and F. Wu (2005), Kelvin wave variability near the equatorial tropopause observed in GPS
688 radio occultation measurements, J. Geophys. Res., 110, D03102, doi:10.1029/2004JD005006.
689 Randel, W. J., F. Wu, H. Vömel, G. E. Nedoluha, and P. Forster (2006), Decreases in stratospheric water
690 vapor after 2001: Links to changes in the tropical tropopause and the Brewer-Dobson circulation, J.
691 Geophys. Res., 111, D12312, doi:10.1029/2005JD006744.
692 Reverdy, M., Noel, V., Chepfer, H., and Legras, B.: On the origin of subvisible cirrus clouds in the tropical
693 upper troposphere, Atmos. Chem. Phys., 12, 12081-12101, https://doi.org/10.5194/acp-12-12081-
694 2012, 2012.
695 Read, W. G., et al. (2007), Aura Microwave Limb Sounder upper tropospheric and lower stratospheric H2O
696 and relative humidity with respect to ice validation, J. Geophys. Res., 112, D24S35, doi:
697 10.1029/2007JD008752.
698 Riihimaki, L. D., and S. A. McFarlane (2010), Frequency and morphology of tropical tropopause layer
699 cirrus from CALIPSO observations: Are isolated cirrus different from those connected to deep
700 convection?, J. Geophys. Res., 115, D18201, doi:10.1029/2009JD013133.
701 Sassen, K., M. K. Griffen, and G. C. Dodd (1989): Optical scattering and microphysical properties of
702 subvisual cirrus clouds, and implications, J. Appl. Meteorol., 28, 91–98.
703 Schoeberl M. R., A. E. Dessler, T. Wang, M. A. Avery, and E. J. Jensen (2014), Cloud formation,
704 convection, and stratospheric dehydration, Earth and Space Science, 1, 1–17, doi:
705 10.1002/2014EA000014.
706 Schwartz, M. J., et al. (2008), Validation of the Aura Microwave Limb Sounder temperature and
707 geopotential height measurements, J. Geophys. Res., 113, D15S11, doi:10.1029/2007JD008783.
708 Stephens, G.L., D.G. Vane, R.J. Boain, G.G. Mace, K. Sassen, Z. Wang, A.J. Illingworth, E.J. O'connor,
709 W.B. Rossow, S.L. Durden, S.D. Miller, R.T. Austin, A. Benedetti, C. Mitrescu (2002): THE
710 CLOUDSAT MISSION AND THE A-TRAIN. Bull. Amer. Meteor. Soc., 83, 1771–1790,
711 https://doi.org/10.1175/BAMS-83-12-1771
712 Taylor, J. R., Randel, W. J., and Jensen, E. J.: Cirrus cloud-temperature interactions in the tropical
713 tropopause layer: a case study, Atmos. Chem. Phys., 11, 10085-10095, https://doi.org/10.5194/acp-11-
714 10085-2011, 2011.
715 Vaughan, M. A., et al. (2005), CALIOP Algorithm Theoretical Basis Document, Part 2: Feature Detection
716 and Layer Properties Algorithms, available at https://www-calipso.larc.nasa.gov/resources/pdfs/PC-
717 SCI-202_Part2_rev1x01.pdf.
718 Vaughan, M.A., K.A. Powell, D.M. Winker, C.A. Hostetler, R.E. Kuehn, W.H. Hunt, B.J. Getzewich, S.A.
719 Young, Z. Liu, and M.J. McGill (2009), Fully Automated Detection of Cloud and Aerosol Layers in
720 the CALIPSO Lidar Measurements. J. Atmos. Oceanic Technol., 26, 2034–2050,
721 https://doi.org/10.1175/2009JTECHA1228.1
722 Virts, K.S., J.M. Wallace, Q. Fu, and T.P. Ackerman, 2010, Tropical Tropopause Transition Layer Cirrus as
723 Represented by CALIPSO Lidar Observations. J. Atmos. Sci., 67, 3113–3129,
724 https://doi.org/10.1175/2010JAS3412.1
725 Wang, C., P. Yang, B. A. Baum, S. Platnick, A. K. Heidinger, Y. Hu, and R. E. Holz (2011), Retrieval of ice
726 cloud optical thick ness and effectiveparticle size using a fast infrared radiative transfer m odel, J.
727 Appl. Meteorol. Climatol., 50(11), 2283–2297, doi:10.1175/JAMC-D-11-067.1.
728 Wang, P.-H., P. Minnis, M.P. McCormick, G. S. Kent, and K. M. Skeens (1996), A 6-year climatology of
729 cloud occurence frequency from Stratospheric Aerosol and Gas Experiment II observations (1985-
730 1990), J. Geophys. Res., 101, 29,407-29,429.
731 Wang, T., and A. E. Dessler (2012), Analysis of cirrus in the tropical tropopause layer from CALIPSO and
732 MLS data: A water perspective, J. Geophys. Res., 117, D04211, doi: 10.1029/2011JD016442.
733 Winker, D. M. and Trepte, C. R. (1998): Laminar cirrus observed near the tropical tropopause by LITE,

734 Geophys. Res. Lett., 25, 3351–3354.
735 Winker, D. M., Pelon, J., and McCormick, M. P. (2003): The CALIPSO mission: Spaceborne lidar for
736 observation of aerosols and clouds, Proc. SPIE, 4893, 1–11.
737 Winker, D. M., W. H. Hunt, and M. J. McGill (2007): Initial performance assessment of CALIOP, Geophys.
738 Res. Lett., 34, L19803, doi:10.1029/2007GL030135.
739 Wu, D. L., W. G. Read, A. E. Dessler, S. C. Sherwood, and J. H. Jiang (2005), UARS MLS cloud ice
740 measurements and implications for H2O transport near the tropopause, J. Atmos. Sci., 62, 518–530.
741 Wu, D. L., et al. (2009), Comparisons of global cloud ice from MLS, CloudSat, and correlative data sets, J.
742 Geophys. Res., 114, D00A24, doi:10.1029/2008JD009946.
743 Wu, D.L., A. Lambert, W.G. Read, P. Eriksson, and J. Gong (2014), MLS and CALIOP Cloud Ice
744 Measurements in the Upper Troposphere: A Constraint from Microwave on Cloud Microphysics. J.
745 Appl. Meteor. Climatol., 53, 157–165, https://doi.org/10.1175/JAMC-D-13-041.1
746 Ye, H., Dessler, A. E., and Yu, W. (2018), Effects of convective ice evaporation on interannual variability of
747 tropical tropopause layer water vapor, Atmos. Chem. Phys., 18, 4425-4437,
748 https://doi.org/10.5194/acp-18-4425-2018.
749 Yulaeva, E., J. R. Holton, and J. M. Wallace (1994), On the cause of the annual cycle in tropical lower-
750 stratospheric temperatures, J. Atmos. Sci., 51(2), 169–174.
751 Zhou, C., Yang, P., Dessler, A. E., Hu, Y., & Baum, B. A. (2012). Study of horizontally oriented ice crystals
752 with CALIPSO observations and comparison with Monte Carlo radiative transfer simulations. Journal
753 of Applied Meteorology and Climatology, 51(7), 1426–1439. https://doi.org/10.1175/JAMC-D-11-
754 0265.1
755 Zhou, C., A. E. Dessler, M. D. Zelinka, P. Yang, and T. Wang (2014), Cirrus feedback on interannual
756 climate fluctuations, Geophys. Res. Lett., 41, doi:10.1002/2014GL062095.